

Polarized radiation coming from the spreading layer of the weakly magnetized neutron stars

Anna Bobrikova¹, Juri Poutanen¹, and Vladislav Loktev^{1,2}

¹ Department of Physics and Astronomy, 20014 University of Turku, Finland
e-mail: anna.a.bobrikova@utu.fi

² Department of Physics, P.O. Box 64, 00014 University of Helsinki, Finland

Received 24 September 2024 / Accepted XXX

ABSTRACT

Observations show that the X-ray emission of the accreting weakly magnetized neutron stars is polarized. Here, we develop a theoretical model, where we assume the emission of the accreting neutron star coming from the spreading layer, the extension of the boundary between the disk and the neutron star surface onto the surface. We then calculate the Stokes parameters of the emission accounting for relativistic aberration and gravitational light bending in the Schwarzschild metric. We show that regardless of the geometry, for the spreading layer we cannot expect the polarization degree to be higher than 1.5%. Our results have implications with regard to the understanding of the X-ray polarization from weakly magnetized neutron stars observed with the Imaging X-ray Polarimetry Explorer and the future enhanced X-ray Timing and Polarimetry mission.

Key words. accretion, accretion disks – methods: analytical – polarization – stars: neutron – X-rays: binaries

1. Introduction

Weakly magnetized neutron stars (WMNSs) in the low-mass X-ray binary systems (LMXBs) are among the brightest X-ray sources. The neutron stars (NSs) in these systems emit mostly due to the accretion of matter leaking from the companion star which fills its Roche lobe. The emission of these sources is highly variable due to the outbursts and rapid changes in the geometry of the system and is a subject of thorough research.

The emission mechanism of WMNSs has been indirectly studied for decades. Spectroscopic results obtained in X-ray and radio bands allowed scientists to conclude that the emission comes mostly from the accretion disk formed around the neutron star and from a Comptonized component, which can be a boundary layer (BL) between the disk and the NS surface (Shakura & Sunyaev 1988) or a spreading layer (SL), a layer of accreted matter distributed over the surface of NS (see e.g. Lapidus & Sunyaev 1985; Inogamov & Sunyaev 1999). Timing observations added more information about the QPOs in these systems: observable both in Hz and kHz regions (van der Klis 1989, 2000), they are currently associated with the events happening near the surface of the NS. However, the exact geometry of the sources remains unknown.

Polarimetric studies add two more measurable variables to the data sets we obtain from the sources. With the launch of Imaging X-ray Polarimetry Explorer (IXPE, Weisskopf et al. 2022) in December 2021, we are for the first time capable of measuring with high precision the polarization degree (PD) and polarization angle (PA) of the WMNS emission. When measured with a sufficient confidence level, these variables can shed new light on the emission mechanisms, the geometry of the source, and the interactions the light experiences on the way from the emitting region to the observer.

Thirteen sources have been observed with IXPE in the last two years, each providing answers and new questions. From an upper limit in GS 1826–238 (Capitanio et al. 2023) to an 11 σ polarization detection in GX 340+0 Bhargava et al. (2024), we saw a broad variety of complex phenomena in all the sources. For some of the sources, we were able to compare the recent observations with previous results: in Cyg X-2 (Farinelli et al. 2023), the agreement between IXPE and Orbiting Solar Observatory 8 (OSO-8, Mitchell et al. 1976) is reported, while in Sco X-1 (La Monaca et al. 2024), a discrepancy between the archive and recent observations is introduced. We saw an increase in PD with energy in GX 9+9 (Ursini et al. 2023), 4U 1624–49 (Saade et al. 2024), and 4U 1820–303 (Di Marco et al. 2023); PD is increasing from the soft state to the hard state in XTE 1701–462 (Cocchi et al. 2023) and GX 5–1 (Fabiani et al. 2024). Significant variability of the PA with time and/or energy was observed in Cir X–1 Rankin et al. (2024) and GX 13+1 Bobrikova et al. (2024b). Various interpretations, such as scattering in the relativistic wind, tilted star, and precession of the rotation axis, were suggested for all these phenomena. Yet, space is left for further investigation.

To understand the polarimetric data, we need to have expectations regarding the PA and PD values of the emission coming from different parts of the source, such as disk, BL, and SL. The polarization of the disk emission has been studied in detail (see e.g. Dovčiak et al. 2008; Li et al. 2009; Loktev et al. 2022). Lapidus & Sunyaev (1985), among other authors, gave an estimation of the SL emission and its polarization.

In the current article, we present a detailed analytical study of the thermal emission coming from the SL. We calculate the emission of the rapidly moving SL and use the Schwarzschild description of the light bending to account for the relativistic effects. We then apply the results of the rotating vector model to

The observed specific intensity can be related to the intensity measured in the co-rotating frame as

$$I_E = \left(\frac{E}{E'}\right)^3 I'_{E'}(\alpha', \theta), \quad (9)$$

where the ratio of energies combines gravitational redshift and the Doppler effect

$$\frac{E}{E'} = \delta \sqrt{1 - u}, \quad (10)$$

The local intensity $I'_{E'}$ depends on the zenith angle α' measured in the corotating frame of the element, accounting for the angular distribution of the seed photons in the electron-scattering dominated semi-infinite atmosphere (Chandrasekhar 1960; Sobolev 1963):

$$I_E(\mu, E) = \frac{1}{f_c^4} B_E(f_c T_{\text{eff}})(0.421 + 0.868\mu), \quad (11)$$

where f_c is the color correction, B_E is the Planck function and the T_{eff} corresponds to the temperature of the seed photons.

The Doppler factor

$$\delta = \frac{1}{\gamma(1 - \beta \cos \xi)} \quad (12)$$

depends on the SL velocity at this co-latitude relative to the external non-rotating frame, and the Lorentz factor is

$$\gamma(\theta) = \frac{1}{\sqrt{1 - \beta^2(\theta)}}. \quad (13)$$

The angle α' in Eq. (9) the photon momentum makes to the normal direction as measured in the co-rotating frame of the spot is related to the similar angle measured in the static frame as

$$\cos \alpha' = \delta \cos \alpha. \quad (14)$$

We finally obtain the observed flux from the surface element

$$dF_E = \frac{R^2}{D^2} \cos \alpha \mathcal{D} (\delta \sqrt{1 - u})^3 I'_{E'}(\alpha', \theta) d \cos \theta d\phi. \quad (15)$$

To describe the polarimetric properties of the SL emission, we introduce the Stokes vector:

$$\begin{pmatrix} F_I \\ F_Q \\ F_U \end{pmatrix} = F_E \begin{pmatrix} 1 \\ P \cos 2\chi \\ P \sin 2\chi \end{pmatrix}. \quad (16)$$

where P is the observed PD, and χ is the observed PA, which both depend on energy.

Locally at the surface element, we set the P_s as in the optically thick electron scattering dominated plain parallel slab atmosphere (Chandrasekhar 1960):

$$P_s(\mu) = -\frac{1 - \mu}{1 + 3.582\mu} 0.1171, \quad (17)$$

where $\mu = \cos \alpha'$. The corresponding PA χ is calculated as in Poutanen (2020):

$$\tan \chi = \frac{\sin \theta \sin \phi + \beta A}{-\sin i \cos \theta + \cos i \sin \theta \cos \phi - \beta \sin \phi C}, \quad (18)$$

where

$$\begin{aligned} A &= \frac{\sin \psi}{\sin \alpha} B + \frac{\cos \alpha - \cos \psi}{\sin \alpha \sin \psi} (\cos \phi - B \cos \psi), \\ B &= \sin i \sin \theta + \cos i \cos \theta \cos \phi, \\ C &= \frac{\sin \psi}{\sin \alpha} \cos \theta + \frac{\cos \alpha - \cos \psi}{\sin \alpha \sin \psi} (\cos i - \cos \theta \cos \psi). \end{aligned} \quad (19)$$

When calculating the observed PD and PA of the whole SL emission, in every energy bin we define

$$P_{\text{obs}} = \frac{\sqrt{F_Q^2 + F_U^2}}{F_I}. \quad (20)$$

and

$$\sin(2\chi_{\text{obs}}) = F_U/F_I, \quad \cos(2\chi_{\text{obs}}) = F_Q/F_I. \quad (21)$$

3. Results for various geometries

The formalism derived in Sect. 2 can be now applied to the various geometries of the SL and the binary system. In Figs. 2-6, the dependence of the dimensionless luminosity $x l_x$, PD, and PA on dimensionless energy x are shown. These dimensionless parameters are chosen for a better representation of the features and for generality and are derived as follows:

$$x = \frac{E}{k_B T_{\text{eff}}}, \quad (22)$$

where k_B is the Boltzmann constant, and

$$\begin{aligned} x l_x &= \frac{x 4\pi D^2 F_x}{\sigma_{\text{SB}} T_{\text{eff}}^4 R^2 S} = \frac{60}{\pi^4 f_c^4} \iint_S \cos \alpha \mathcal{D} (\delta \sqrt{1 - u})^4 \times \\ &\quad \times (0.421 + 0.868\mu) \frac{x^4}{e^{x/f_c} - 1} d \cos \theta d\phi. \end{aligned} \quad (23)$$

Here S is added for the normalization of the dimensionless luminosity on the surface area of the SL.

3.1. Basic geometries: sphere, half-sphere, and 1-degree rings.

We start with the most basic geometrical models and explore the emission coming from a SL shaped as a sphere, half-sphere, and a thin ring of 1° width. Studying these basic cases can support our general understanding of the SL emission and its polarization. The equatorial velocity of the plasma flow in the SL β_{eq} is fixed here at the value of 0.35 ($\tilde{A} = 0.83$).

We first look at the emission coming from the whole sphere (Fig. 2a) for different inclination angles noted in the plot. The emission, apart from the energies above the peak in the luminosity, is not polarized, independent of the inclination, as the problem is almost symmetric. The increase in PD is connected to the exponential cutoff in the spectrum of the SL and the Doppler effect. Relativistic rotation of the SL increases the observed energy of the light coming from the part of the SL where the matter flows toward the observer. As the light coming from that part of the SL is polarized, we see an increase in PD. This pattern is also more visible for higher inclinations due to the direction of the matter flow being parallel to the equator of the NS. The most peculiar thing here is the variation of the PA with energy: in the extreme case of inclination $i = 90^\circ$ (red lines), we see three 'steps', and for the smaller inclinations, the pattern is smoothed.

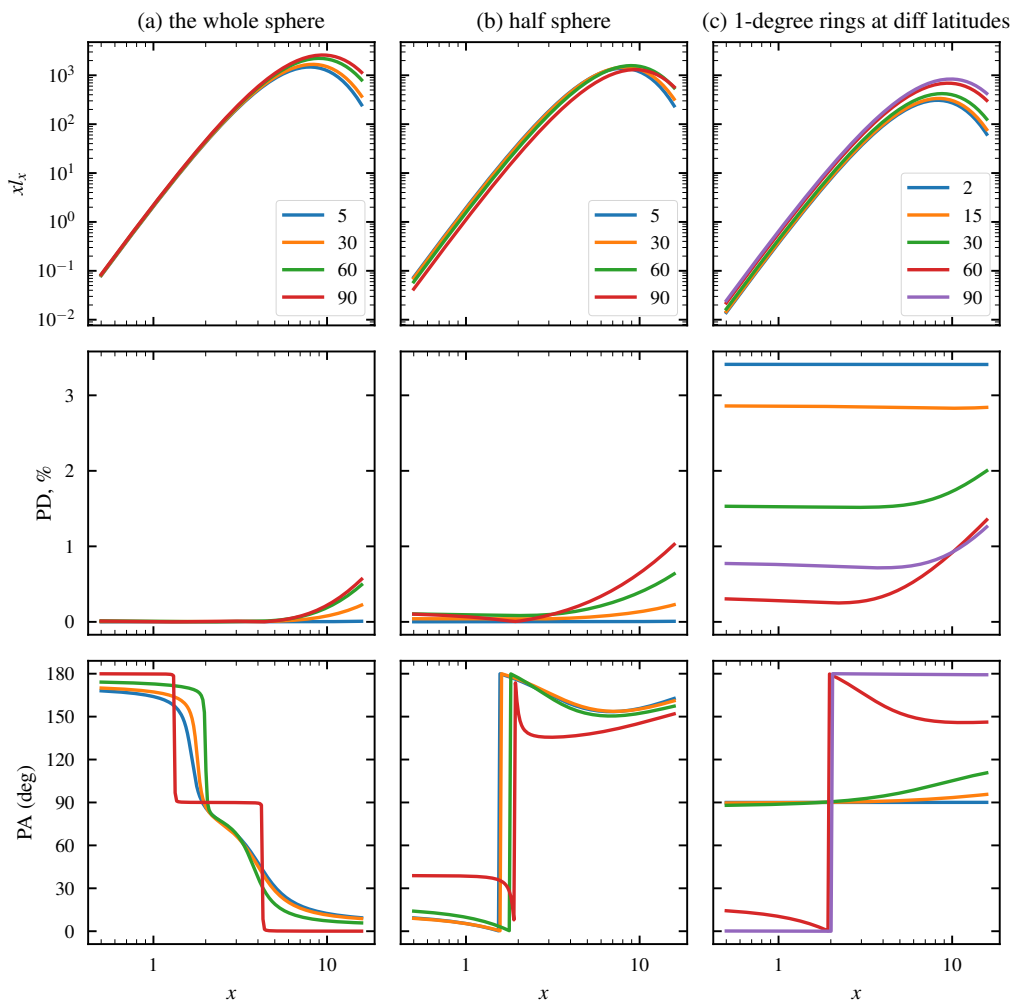


Fig. 2. Dimensionless luminosity xI_x , PA, and PD as functions of the dimensionless photon energy, $x = E/kT_{\text{eff}}$. For all the cases presented, $\beta = 0.35$. Panel a: emission coming from the whole sphere, observed from different inclinations; blue, orange, green, and red lines correspond to an inclination of 5°, 30°, 60°, and 90°, respectively. Panel b: emission coming from the half-sphere, inclinations same as in Panel a. Panel c: emission coming from 1° rings with different co-latitudes; blue, orange, green, red, and violet lines correspond to the co-latitude of 2°, 15°, 30°, 60°, and 90°, respectively.

These ‘steps’ appear also due to the Doppler effect: at lower energies, we see mostly the emission coming from the part of the sphere that is flowing away from the observer, and the light coming from that area is polarized perpendicular to the disk plane, so the PA is zero. For the medium energies, the flux is dominated by the observed middle section of the star from the poles to the equator. This light is polarized in the disk plane, so the PA is 90°. At the higher energies, we see the emission from the part of the sphere where matter flows towards the observer. Here we again have a polarization perpendicular to the disk plane, PA is 180°.

Half-sphere is a good approximation when we consider the presence of the accretion disk, as it covers the lower half of the NS (Fig 2b). We now see non-zero PD even for the smallest photon energies. The most significant change between the two cases is in the PA. Let us again have a closer look at the edge-on case (red lines). In general, the polarization from the electron-dominated optically thick cold slab is parallel to the surface of the slab. When looking at the whole sphere, in this symmetric case we, assuming counter-clockwise rotation of the matter, see the left half of the sphere brighter due to the Doppler effect, and

hence expect an overall polarization to be perpendicular to the disk plane for any energies, so PA is zero. For the half-sphere case, however, the quarter of the sphere now dominates the overall picture, so the PA shifts towards 45°. We also see the change of sign at the energy corresponding to the kT_{eff} and a rise at higher energies due to the increasing impact of the Doppler shift.

For the last column of the figure, we consider a small ring with a width of 1° and change its co-latitude (Fig 2c). With the inclination fixed at 90°, we can now see that PD is decreasing with the co-latitude of the ring (with an exceptional case of the ring at 60° which is discussed later). This happens because the emission observed from the normal to the surface is not polarized. For instance, the observer at the inclination of 90° sees the ring at the pole so that each part of it emits horizontally polarized light. At the equator, on the other hand, the emission coming to the observer from the center of the ring is not polarized at all, and this contributes to a further decrease in the overall observed PD. This trend of decrease of PD with co-latitude of the ring, however, breaks for the higher co-latitudes, as we see PD coming from the ring at the equator exceeding PD from the ring at

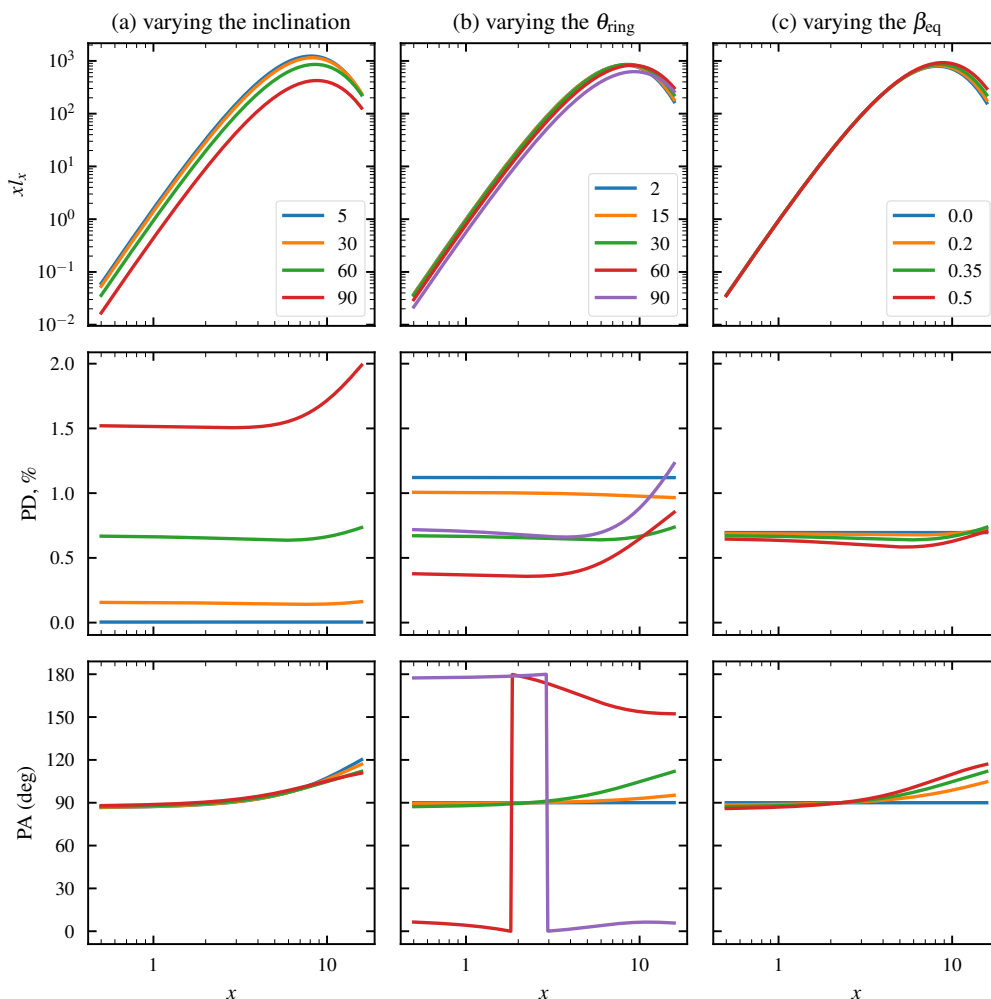


Fig. 3. Dimensionless luminosity xl_x , PA, and PD as functions of the dimensionless photon energy, $x = E/kT_{eff}$. Emission from the 1° ring, fiducial parameter set: $\theta_{ring} = 30^\circ$, $i = 60^\circ$, and $\beta_{eq} = 0.35$. Panel a: varying the inclination; blue, orange, green, and red lines correspond to 5° , 30° , 60° , and 90° inclination, respectively. Panel b: varying the co-latitude of the ring θ_{ring} ; blue, orange, green, red, and violet lines correspond to the co-latitude of 2° , 15° , 30° , 60° , and 90° , respectively. Panel c: varying the equatorial velocity β_{eq} ; blue, orange, green, and red lines correspond to the velocities of 0.0, 0.2, 0.35, and 0.5, respectively.

60° co-latitude. This is because the light from the ring observed at this medium angle is not all horizontally (like at the pole) or vertically (like at the equator) polarized but is a mixture of both, which partly cancel each other. This is also reflected in the PA dependency plot.

3.2. Thin 1-degree rings: detailed study

We now explore in more detail the emission coming from rings of 1° -width. Unless specified otherwise, in this study our fiducial set of parameters is $\theta_{ring} = 30^\circ$, $i = 60^\circ$, and $\beta_{eq} = 0.35$. As we understood the results of the simple cases shown in Fig. 2, with the more complicated cases, we can trust the results of the simulations and switch to the description and interpretation rather than an explanation of the phenomena presented in the plots.

Figure 3a illustrates the differences in the spectra for different inclinations. Same as in the case considered in Fig 2c, increasing the angle between the normal to the surface and the direction to the observer increases the PD. Additionally, we see unpolarized emission if the observer is close to the pole, as

the problem is almost symmetric from that point of view. The change of inclination does not affect PA in this case, we only see differences at higher energies, due to the Doppler effect.

The effect of varying the co-latitude of the ring is shown in Fig. 3b. We again see that the Doppler effect affects the spectrum of the ring more prominently if the ring is closer to the equator, the belt with the highest velocities. We also note that the lowest PD is expected from the ring at the co-latitude $\theta_{ring} = 60^\circ$, which coincides with the inclination in this scenario, as PD turns to zero when looking at the emitting region from the normal to the region.

For the cases presented in Fig. 3c, we change the equatorial velocity. In the non-rotating case (blue line), we see no dependence of PD and PA on energy, and the effect increases with velocity. We also see a slight decrease in the PD with increasing velocity. In all three cases, we see the rotation of the polarization plane by $\approx 30^\circ$.

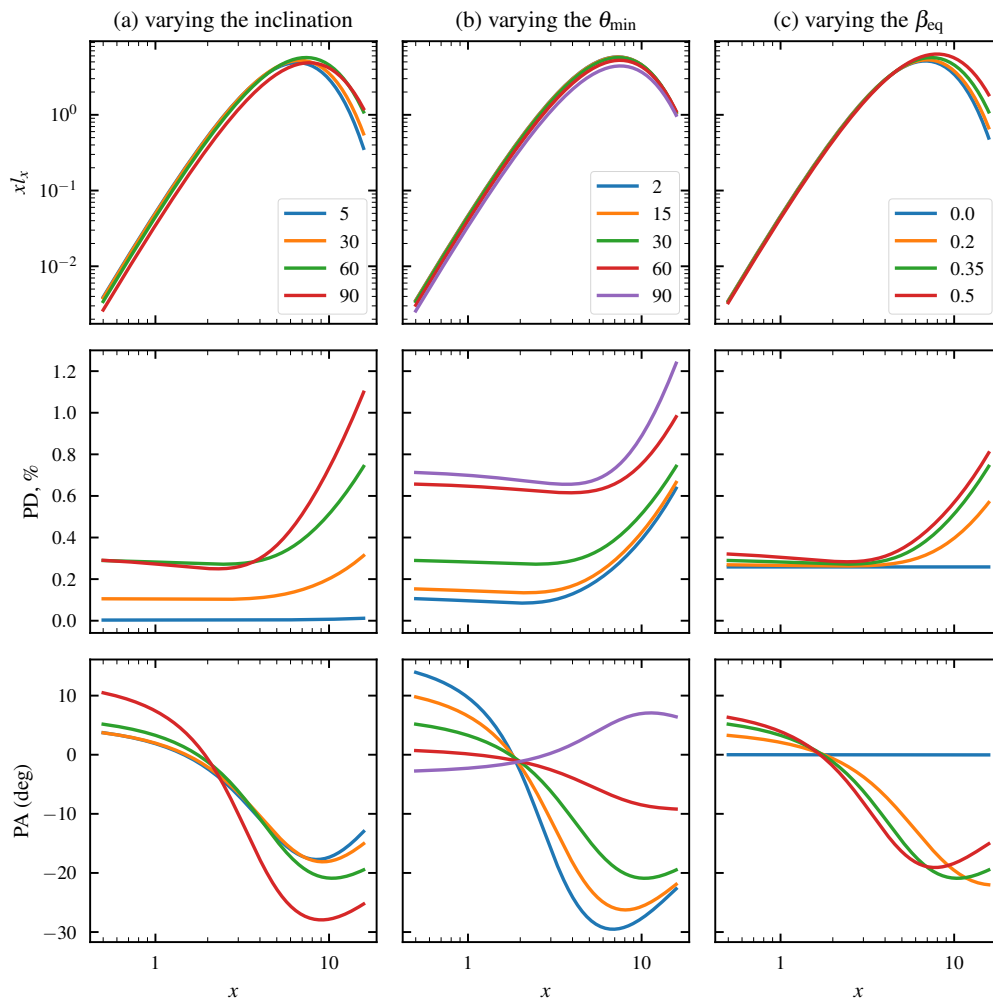


Fig. 4. Same as Fig. 3, but the emission is coming from the broad SL. Fiducial set of parameters $\theta_{\min} = 30^\circ$, $\theta_{\max} = 90^\circ$, $i = 60^\circ$ and $\beta_{\text{eq}} = 0.35$.

3.3. Wide spreading layer

For the next step of our simulations, we now broaden the 1° ring into a wider layer. Unless specified otherwise, in this section we consider the SL with $\theta_{\min} = 30^\circ$, $\theta_{\max} = 90^\circ$, $i = 60^\circ$ and $\beta_{\text{eq}} = 0.35$. Similar to Fig. 3, for Fig.4a, we take the fiducial set and examine the influence of the inclination on the observed emission for different inclinations between 5° and 90° . We again observe that the PD is the highest from 90° . Observing the system virtually from the pole (5° inclination) shows the lowest PD, as the SL appears nearly symmetric from this direction. For the case shown in Fig. 4b, we investigate the dependence on the width of the SL by changing the θ_{\min} from 2° to the values mentioned in the plot. Our dimensionless luminosity is normalized by the surface area of the emitting region, so it does not include the increase of emission intensity with the width of the layer. However, the PD decreases with the width of the layer, as the SL slowly changes from a thin belt to a half-sphere, so the overall polarization averages to lower and lower values. Finally, in Fig. 4c, we change the value of the equatorial velocity of the plasma in the SL. The change in this parameter predominantly affects the flux at the highest energies. We see a significant difference in the PD and PA between a non-rotating case (blue line) and rotating at the Kepler velocity case (red line). In all three

cases presented in Fig. 4, we obtain an up to 40° change in the PA.

4. Results for various physical configurations

In the previous section, we considered various geometrical configurations of both SL and the binary system. For that, we kept the surface temperature, the velocity of the relativistic flow, and the polarization calculations as simple as possible. However, the homogeneous effective surface temperature across the whole accretion flow is not realistic, and neither is the weak dependency of the velocity on θ presented in Sect. 2. Chandrasekhar’s limit on the polarization coming from an infinitely thick slab can also be replaced with exact Thomson scattering calculations. Here, we search for alternative models and test the polarimetric properties of these SLs.

4.1. Inogamov-Sunyaev spreading layer

Inogamov & Sunyaev (1999) introduce the concept of a SL being the most luminous on the edge of the layer, where it reaches the surface of the NS, decelerates, and emits, rather than at the equator of the star, where the gas is assumed to levitate due to extremely high velocity and accretion rate. To match the suggested

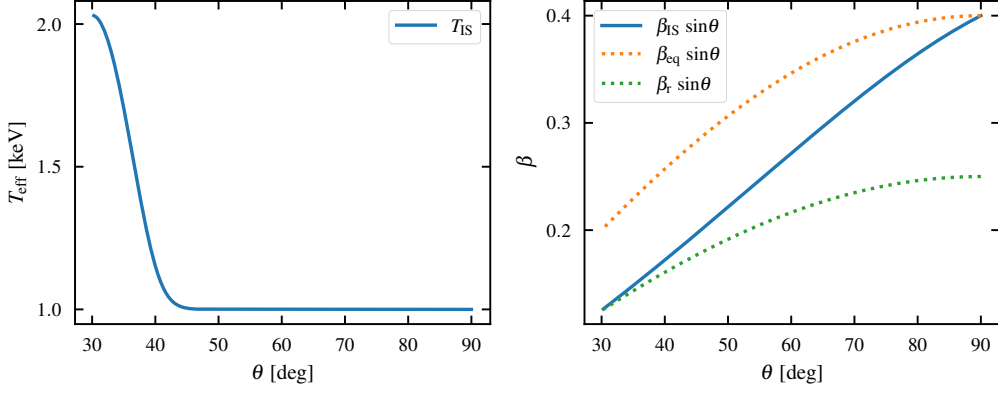


Fig. 5. Velocity of the matter flow and effective temperature of the Inogamov-Sunyaev SL as functions of the co-latitude. Parameters: $\theta_{\text{peak}} = 30^\circ$, $\beta_r = 0.25$, $\beta_{\text{eq}} = 0.4$.

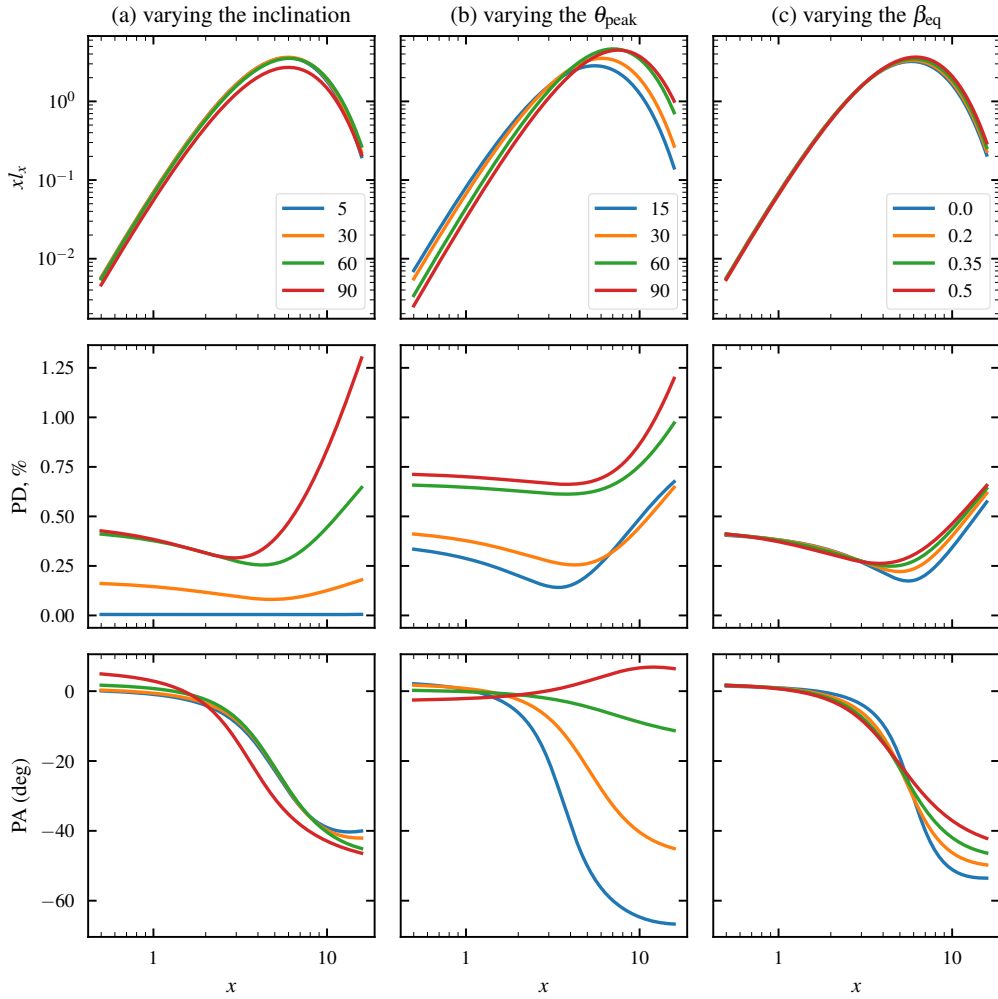


Fig. 6. Dimensionless luminosity x_l_x , PA, and PD as functions of the dimensionless photon energy, $x = E/kT_{\text{eff}}$. Emission from the Inogamov-Sunyaev SL, fiducial parameter set: $\theta_{\text{peak}} = 30^\circ$, $i = 60^\circ$, $\beta_r = 0.25$, and $\beta_{\text{eq}} = 0.4$. Panel a: varying the inclination; blue, orange, green, and red lines correspond to the inclination of 5° , 30° , 60° , and 90° respectively. Panel b: varying the co-latitude of the peak θ_{peak} ; blue, orange, green, and red lines correspond to the co-latitude of 15° , 30° , 60° , and 90° , respectively. Panel c: varying the equatorial velocity β_{eq} ; blue, orange, green, and red lines correspond to the velocities of 0.0, 0.2, 0.35, and 0.5, respectively.

flux profile (as shown in Fig.8 in Inogamov & Sunyaev 1999), we introduce the dependence of the black-body temperature on co-latitude:

$$T_{\text{IS}}^4(\theta) = H(\theta - \theta_{\text{peak}}) \left(T_{\text{min}} + T_{\text{char}} \exp\left(-\frac{(\theta - \theta_{\text{peak}})^2}{2\sigma^2}\right) \right), \quad (24)$$

where H is a Heaviside step function, T_{min} is a temperature of the SL off-peak, T_{char} is a characteristic temperature of the peak emission, and σ parameterizes the width of the peak. This dependence is illustrated in the left panel in Fig. 5. We assume a Gaussian peak at $\theta_{\text{peak}} = 60^\circ$ with a full width at half maximum $\text{FWHM} \approx 2.355\sigma \approx 20^\circ$, $T_{\text{min}} = 1$ keV and $T_{\text{char}} = 2$ keV.

As gas at the equator is assumed to levitate with a velocity corresponding to the one of the accretion disk and slow down closer to the edge of the SL, we also introduce a stronger dependence of the velocity on co-latitude:

$$\beta_{\text{IS}}(\theta) = \left(\beta_{\text{eq}} - \frac{\cos \theta}{\cos \theta_{\text{peak}}} (\beta_{\text{eq}} - \beta_r) \right) \sin \theta, \quad (25)$$

where β_{eq} is the velocity of the SL surface at the equator of the NS, $\beta_r \sin \theta_{\text{peak}}$ is the velocity of the SL surface at the edge of the SL that is associated with the rotation of the NS. This dependence is illustrated in the right panel in Fig. 5. Taking into account these dependencies, dimensionless luminosity given in Eq. (23) is changed accordingly.

The results are presented in Fig.6. We vary the parameters of the SL in the same way as for Figs.3-4. Especially in the (b) column, we see the behavior quite similar to the one shown in Fig.3b. We note the stronger dependency of the PA on energy in this case.

4.2. Optically thin spreading layer

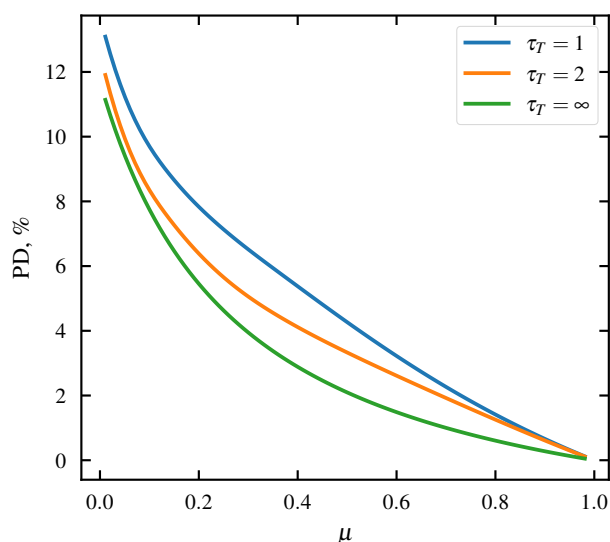


Fig. 7. PD as a function of emission angle $\mu = \cos \alpha'$ for various SL thickness.

In the previous examples, we assumed the SL to be optically thick, and used Eq.(17) for the PD as a function of emission

angle. Instead, we can assume the SL is optically thin, and perform the exact calculation of the Thomson scattering in the SL to estimate the polarization of the emission. The formalism for calculating the polarization from the Thomson scattering is introduced, for example, in Sunyaev & Titarchuk (1985). From our calculations, we learned that the PD as a function of emission angle barely depends on the thickness of the layer. Emission is still polarized in the plane of the SL surface, and the effects of the first few scatterings cancel out, leading to depolarization, as shown in Fig. 7.

High polarization from the Compton scattering is expected, if we only were to observe the photons after they have experienced many scatterings. This is the case in hot Comptonizing regions, where cold optical photons are upscattered to the X-ray range in the Comptonization process, and we only see the significantly upscattered photons in the IXPE range of 2–8 keV. Unfortunately, this is not the case for the WMNS, as we expect the SL to be at a low temperature of 2–3 keV. In this case, we observe all the photons in the same energy range, regardless of the number of scatterings they went through. As is shown, for instance, in Fig. 2 Viironen & Poutanen (2004), the PD of the photon changes sign depending on the number of scatterings it experienced. This is why, if we see them all in the same energy range, we expect an overall low polarization regardless of the optical depth.

5. Applications

In the last two years, IXPE has observed more than ten WMNSs. The model presented in this paper gave valuable insights that supported the interpretation of the observation results. Firstly, from the simulations we learned that the emission of the SL is polarized in the plane perpendicular to the accretion disk, while for the disk it is known that the emission is polarized in the plane of the disk. In the spectrum of the WMNS, we usually see two main components, of which the softer one is interpreted as the emission of the disk, while the harder one comes from the BL or the SL. So, if a source presents a strong dependency of the PA on energy, we assumed that the harder component of the spectrum comes from the SL rather than the BL which produces polarization similar to the one of the disk. This was the case, for instance, in the case of Cyg X-2 (Farinelli et al. 2023). However, in this source, the estimated PD from the harder component was about 4%, which is much higher than the PD we see in our simulations.

On the other hand, in the cases of Sco X-1 (La Monaca et al. 2024), 4U 1820–303 (Di Marco et al. 2023), or GX 13+1 (Bobrikova et al. 2024b,a), a clear absence of PA rotation with energy suggested that the SL, at least in our model, cannot be responsible for the harder component of the spectrum. The most peculiar case of the Cir X-1 (Rankin et al. 2024) required a complicated explanation of the observed phenomena, but the authors concluded that the Comptonized component of the spectrum could come from the SL in the hard state of the source, while in the soft state, the Comptonized emission could come from the BL. In the sources GX 9+9 (Ursini et al. 2023), GX 5–1 (Fabiani et al. 2024), and XTE J1701–462 (Cocchi et al. 2023), the misalignment in the PA of the two components was found, but the statistics did not allow to properly constrain the shift in the PA. There is no clear conclusion about the geometry of these sources.

The model supports the data interpretation, yet it is not fully capable of explaining the observed phenomena, even if the assumption about the presence of the SL in the source is made. It is often considered that the SL emission can be further scattered

in the wind above the disk or reflected from the disk, which could lead to a higher PD of the emission. Observational results leave much space for further improvements to the current SL model.

6. Summary

In this paper, we develop a theoretical model for the emission coming from the SL of the WMNS. We derive exact analytic expressions for the Stokes parameters of the emission. We account for the SR effects and light bending when calculating the PA.

We compute the emission coming from the source with various geometry of the SL, accounting for the velocity of matter. We study the impact of the inclination, matter velocity, and the geometrical configuration of the SL on the polarization of the observed emission. We calculate the polarization coming from the Inogamov-Sunyaev SL, where both the velocity of the matter and the intensity of the emission are functions of co-latitude.

We show that for all the tested scenarios, the PD of the emission does not exceed 1.5%. Recent observations of the IXPE satellite show that WMNSs emit light with stronger polarization, especially at higher energies. Hence, the SL, at least the current model, cannot be the only mechanism to explain the data. Higher polarization of the harder component of the WMNS spectrum can come from the reflection of the SL emission from the disk, scattering of the SL emission in the wind above the accretion disk, the emission coming from the jet, and others. Deriving the analytical models for these mechanisms can be the next step for further investigation of WMNSs. We also note the significant variability of PA with energy that can be observed in the emission of the SL.

The developed model can support the IXPE data analysis, and it was successfully used to interpret the already existing results of IXPE. Combined with other tools and methods, it can shed new light on the geometry of the WMNSs and their emission mechanisms.

Acknowledgements. This research was supported by the Academy of Finland grant 333112, and the grants 002200175 and 00240328 of the Finnish Cultural Foundation (AB).

References

- Beloborodov, A. M. 2002, *ApJ*, 566, L85
 Bhargava, Y., Ng, M., Zhang, L., et al. 2024, arXiv e-prints, arXiv:2405.19324
 Bobrikova, A., Di Marco, A., La Monaca, F., et al. 2024a, *A&A*, 688, A217
 Bobrikova, A., Forsblom, S. V., Di Marco, A., et al. 2024b, *A&A*, 688, A170
 Bogdanov, S., Lamb, F. K., Mahmoodifar, S., et al. 2019, *ApJ*, 887, L26
 Capitanio, F., Fabiani, S., Gnarini, A., et al. 2023, *ApJ*, 943, 129
 Chandrasekhar, S. 1960, *Radiative transfer* (New York: Dover)
 Cocchi, M., Gnarini, A., Fabiani, S., et al. 2023, *A&A*, 674, L10
 Di Marco, A., La Monaca, F., Poutanen, J., et al. 2023, *ApJ*, 953, L22
 Dovčiak, M., Muleri, F., Goosmann, R. W., Karas, V., & Matt, G. 2008, *MNRAS*, 391, 32
 Fabiani, S., Capitanio, F., Iaria, R., et al. 2024, *A&A*, 684, A137
 Farinelli, R., Fabiani, S., Poutanen, J., et al. 2023, *MNRAS*, 519, 3681
 Farinelli, R., Waghmare, A., Ducci, L., & Santangelo, A. 2024, *A&A*, 684, A62
 Gnarini, A., Ursini, F., Matt, G., et al. 2022, *MNRAS*, 514, 2561
 Inogamov, N. A. & Sunyaev, R. A. 1999, *Astronomy Letters*, 25, 269
 La Monaca, F., Di Marco, A., Poutanen, J., et al. 2024, *ApJ*, 960, L11
 Lapidus, I. I. & Sunyaev, R. A. 1985, *MNRAS*, 217, 291
 Li, L.-X., Narayan, R., & McClintock, J. E. 2009, *ApJ*, 691, 847
 Loktev, V., Veledina, A., & Poutanen, J. 2022, *A&A*, 660, A25
 Mitchell, D., Rochwarger, I., Sackson, M., Bischoff, G., & Bodine, O. 1976, *IEEE Transactions on Nuclear Science*, 23, 480
 Poutanen, J. 2020, *A&A*, 639, A33
 Poutanen, J. & Beloborodov, A. M. 2006, *MNRAS*, 373, 836
 Rankin, J., La Monaca, F., Di Marco, A., et al. 2024, *ApJ*, 961, L8
 Saade, M. L., Kaaret, P., Gnarini, A., et al. 2024, *ApJ*, 963, 133
 Salmi, T., Nättilä, J., & Poutanen, J. 2018, *A&A*, 618, A161

- Shakura, N. I. & Sunyaev, R. A. 1988, *Adv. Space Res.*, 8, 135
 Sobolev, V. V. 1963, *A treatise on radiative transfer* (Princeton: Van Nostrand)
 Suleimanov, V. F., Poutanen, J., & Werner, K. 2020, *A&A*, 639, A33
 Sunyaev, R. A. & Titarchuk, L. G. 1985, *A&A*, 143, 374
 Ursini, F., Farinelli, R., Gnarini, A., et al. 2023, *A&A*, 676, A20
 van der Klis, M. 1989, *ARA&A*, 27, 517
 van der Klis, M. 2000, *ARA&A*, 38, 717
 Viironen, K. & Poutanen, J. 2004, *A&A*, 426, 985
 Weisskopf, M. C., Soffitta, P., Baldini, L., et al. 2022, *JATIS*, 8, 026002